Madden-Julian Oscillation: the 3–D view from satellites

Philip W. Mote

NorthWest Research Associates, Redmond, Washington; Oregon Climate Change Research Institute and College of Oceanic and Atmospheric Sciences, Oregon State University, Corvallis

Robert Wood

Department of Atmospheric Sciences, University of Washington, Seattle

Andrew Gettelman

National Center for Atmospheric Research, Boulder, Colorado

P.W. Mote, NorthWest Research Associates, PO Box 3027, Bellevue WA 98009 (mote@nwra.com, pmote@coas.oregonstate.edu)

R. Wood, Dept. of Atmos. Sci., Box 351640, Univ. of Wash., Seattle WA 98195 (robwood@atmos.washington.edu)

A. Gettelman, National Center for Atmospheric Research, Boulder CO 80307 (andrew@ucar.edu)

3D VIEW OF THE MADDEN-JULIAN OSCILLATION

Abstract. Using a variety of data sources, we provide an integrated view of clouds, water vapor, and atmospheric dynamics associated with the tropical Madden-Julian Oscillation (MJO) during 2001-2004. Passage of convective anomalies associated with the MJO have clear signatures in temperature, moisture, and winds from the surface to the tropopause; and also in two-dimensional fields of cloud top temperature, cloud fraction, cloud optical thickness, sea surface temperature, and more. Several moist fields show no response to MJO, including cloud effective radius and liquid water path. Consideration of three-dimensional temperature, moisture, and moist static energy anomalies associated with the MJO clearly shows "preconditioning" of the atmosphere ahead of an eastward-propagating event, in which a buildup of moist static energy in the boundary layer — related to anomalies in cloudiness, evaporation, sea surface temperature, and low-level winds — provides the conditions for convective anomalies to be enhanced.

02/02/09

1. Introduction

Patterns of atmospheric variability include those that are phase-locked to periodic forcing (tides, seasonal cycle) and several that exhibit quasi-periodic behavior despite being a response to forcing on very different timescales (e.g., El Niño-Southern Oscillation and Quasi-Biennial Oscillation). On timescales of 1–2 months, the tropical intraseasonal oscillation or Madden-Julian oscillation (MJO) influences not only tropical precipitation but also events farther afield, including the south Asian summer monsoon [e.g., *Madden and Julian*, 1994]; landfalling tropical cyclones in the eastern Pacific, Atlantic, and Caribbean [*Maloney and Hartmann*, 2000]; and flooding in the Pacific Northwest [*Bond and Vecchi*, 2003]. For an excellent review of MJO see *Zhang* [2005]. The potential predictability of the MJO on timescales much longer than the usual limit of deterministic predictability of the atmosphere [e.g., *Lo and Hendon*, 2000], combined with its societal impacts, render the MJO a promising and societally relevant field of study.

Complementing the original station-based description of the MJO [*Madden and Julian*, 1971], previous large-scale studies of the MJO with satellite observations have identified coherent variations in outgoing longwave radiation [*Lau and Chan*, 1983], tropical upper tropospheric water vapor [*Mote et al.,* 2000; *Sassi et al.,* 2002], water vapor and cirrus clouds [*Eguchi and Shiotani,* 2004], and 3–d

55 temperature and water vapor [*Tian et al.,* 2006]. MJO events propagate eastward with two distinctly different characters: slowly (~5 m/s) with convective coupling in the eastern hemisphere where convection is prevalent on the equator, and rapidly (~30 m/s) as a dry feature in the western hemisphere where convection is less common [*Zhang*, 2005]. The fast dry feature can be identified with an equatorially trapped atmospheric Kelvin wave [e.g., *Cho et al.,* 1994], but the dynamics of the 60 slow moist phase of the MJO are incompletely understood, and the MJO is almost without exception poorly simulated by global atmospheric models, with intraseasonal anomalies typically too weak and propagating too fast [*Zhang*, 2005].

In addition to the descriptive studies just mentioned, *Lin and Mapes* [2004] analyzed the radiation 65 budget of the MJO using data from the Earth Radiation Budget Experiment (ERBE). They found that radiative heating of the atmosphere, atmospheric water vapor, cloud top height, and cloud optical depth were all enhanced when the MJO enhanced convection, and were all suppressed approximately 20 days before and after the peak of an MJO event.

70 A series of satellites launched by the National Aeronautics and Space Administration (NASA) and space agencies of other nations have provided an unprecedented view of the tropical atmosphere. The Terra satellite includes the Moderate Resolution Imaging Spectroradiometer (MODIS) whose numerous infrared and near-infrared channels provide richly detailed information about tropical clouds

and water vapor. The Aqua satellite includes the Atmospheric Infrared Sounder (AIRS), Advanced Microwave Scanning Radiometer (AMSR), and a second MODIS instrument. Another NASA satellite, Quikscat, measures surface winds. It is now possible to combine and compare disparate types of measurements that either were not jointly available from the same platform or were not available at all. In this paper, observations of clouds, water vapor, temperature, OLR, sea surface temperature, vector wind, and other atmospheric observables are jointly analyzed to characterize the spatiotemporal relationships among these observables in a series of MJO events during 2001-2004, especially during the active period November 2002 through February 2003. This work builds on, and addresses some flaws in, the regression analysis presented by *Tian et al.* [2006], who analyzed AIRS temperature and water vapor data.

2. Data sources

2.1 MODIS Data

A MODIS instrument [*Barnes et al.,* 1998] flies on both Terra and Aqua. Launched on December 18, 1999, Terra is a sun-synchronous polar orbiting satellite at 705 km altitude that crosses the equator southward (descending) at 1030 local time (LT) and again northward (ascending) at 2230 LT. Terra MODIS began collecting data in late February 2000. Aqua was launched May 4, 2002 and is in a similar orbit but with crossing times at 0130 and 1330 LT. Aqua is the lead satellite in the so-called A-

train, a string of six satellites flying in a line a few minutes apart [*Stephens et al.,* 2002]. For this study we only use MODIS data from Terra.

MODIS has 36 spectral bands from 0.415μm to 14.235μm; of these, 26 bands are used for atmospheric sensing [*Barnes et al.,* 1998]. Cloud products include cloud top pressure, cloud top temperature (derived from cloud top pressure using a suitable temperature profile), and effective emissivity, all from the 11μm and CO_2 bands (31–36); and cloud optical thickness, particle effective radius, and water path, from bands in the visible, near infrared, shortwave infrared and medium-wave infrared (bands 1, 2, 5, 6, 7, and 20) [*Platnick et al.,* 2003].

In order to enable large-scale studies such as this one, the retrieved quantities (Level 2), which have a resolution ranging from 250m to 1km, are assembled into $1^\circ \times 1^\circ$ bins on a regular latitude-longitude grid (Level 3, or L3). Various statistics summarize the variability of the thousands of pixels that comprise a single L3 bin: mean, minimum, maximum, and standard deviation, and often quality-weighted versions of the same statistics. Level 3 data are available as daily, 8-day, and monthly products. Some fields (e.g., water vapor-near IR) require reflected sunlight and hence are derived only in daytime; others (e.g., cloud top pressure) are derived for both day and night, and are available both separately and combined.

Although it is a nadir-viewing instrument, MODIS provides retrievals of atmospheric profiles of temperature, ozone, and water vapor (summed to produce total precipitable water). These profiles are derived using radiances from 12 infrared bands and regression coefficients derived from 8400 radiosonde profiles [*King et al.,* 2003]. This analysis uses the current version of MODIS data, known as Collection 5 [see, e.g., *Yang et al.* 2007].

2.2 AIRS (Aqua)

Like MODIS, the Atmospheric Infrared Sounder (AIRS) measures passive infrared radiances. The key difference is that AIRS uses 2378 spectral channels covering the IR from 3.74μm to 15.4μm, plus four in the visible/near IR (0.4μm to 1.0μm) [*EOS*, 2000]. This very high spectral resolution permits the retrieval of profiles of temperature with a vertical resolution of 1 km, and of moisture at a vertical resolution of 2 km.

Retrievals with AIRS are accomplished in conjunction with the Advanced Microwave Sounding Unit (AMSU) on Aqua. The retrieval follows a multi-step process: microwave-only retrieval, which provides quantities including surface skin temperature and liquid water profiles that are used to inform the cloud-clearing algorithm and the full retrieval, which recursively refines the surface parameters and the temperature and water vapor profiles [*EOS*, 2000].

130 **2.3 AMSR (Aqua)**

AMSR-E (E is for EOS) is a joint project between NASA and the Japan Aerospace Exploration Agency, and flies on the Aqua satellite. The microwave emissivity of the ocean surface is quite a bit less than that of the land surface, so retrievals over land are more difficult and are omitted here.

135 AMSR-E provides nearly complete coverage each day. We use AMSR-E data (version 5) provided by Remote Sensing Systems (RSS), which consists of retrievals over ocean areas only. For this study we use column-integrated water vapor [i.e., water vapor path (WVP); *Wentz,* 1997; *Wentz and Spencer,* 1998] and sea surface temperature (SST) from *Wentz and Meissner* [2000]. Additional information regarding these products is available online at www.remss.com. The data are provided at a resolution 140 of $0.25^\circ \times 0.25^\circ$ grid and averaged up to the common $1^\circ \times 1^\circ$ grid for our analysis. Daily mean fields of each parameter are constructed from the mean of data from both daytime (1330 LST) and nighttime (0130 LST) overpasses. For an additional discussion of the error characteristics of the derived products see *Field and Wood* [2007].

145 **2.4 NCEP/NCAR reanalysis**

Global gridded dynamical fields on a daily timescale are available from the National Center for Environmental Prediction–National Center for Atmospheric Research (NCEP–NCAR) reanalysis

[*Kalnay et al.,* 1996; *Kistler et al.,* 2001]. The reanalysis ingests various observed fields and computes a dynamically consistent state of the atmosphere using a single data assimilation system system throughout the analysis of decades worth of data. Some fields (e.g., upper level winds) are directly observed, but some (e.g., rainfall, not used here) are computed as part of the reanalysis, and are somewhat less reliable.

2.5 Quikscat-NCEP blended surface wind

Surface wind vector data are from the SeaWinds 13.4-GHz microwave scatterometer on the NASA Quikbird sun-synchronous platform. The local overpass times for Quikbird are 0600 and 1800 LST, and we average both passes to provide a daily field. The SeaWinds instrument measures backscatter from wind-driven capillary waves at a number of viewing angles allowing estimates to be made of wind speed and direction with approximately 25-km horizontal resolution. In this study we use the products generated by RSS using the algorithm of *Wentz and Smith* [1999]. The swath width guarantees almost complete daily coverage in the regions studied, and the data products are averaged onto the common $1^{\circ}\times1^{\circ}$ grid as they are for MODIS, AIRS, and AMSR-E. Additional details concerning rain contamination and other uncertainties are found in *Field and Wood* [2007]. For grid points not sampled by the satellite or where rain prevented the retrieval, we linearly interpolate the NCEP–NCAR reanalysis daily mean surface wind field to create a field that is specified everywhere.

2.6 Outgoing longwave radiation

Outgoing longwave radiation (OLR) data come from NOAA polar orbiting satellites and have been subjected to quality control and then interpolated in time and space as described by *Liebmann and Smith* [1996]. The interpolated data are available as daily averages on a $2.5^\circ \times 2.5^\circ$ latitude–longitude grid, and have no missing values.

3. Description of tropical intraseasonal variability

Bandpass filtering all tropical OLR data with half-power points at 20 and 70 days, from the beginning of 1997 to September 2005, we focus on the location with largest intraseasonal variance, 82.5°E, 0.0°N (**Figure** 1). *Wang and Rui* [1990] identified virtually the same location as the point with lowest OLR value at strongest phase of the MJO during the period of their study. The time series in Figure 1 indicates that the largest MJO-related variability during this roughly 9-year period occurred in late 2002. It is rivaled by a period in mid-1997, when the MJO may have helped trigger what turned out to be probably the largest El Niño event of the instrumental period [*McPhaden*, 1999].

To stress the importance of proper bandpass filtering, we apply two filters to the *unfiltered* OLR time series at the reference grid point: our spectrally smooth filter and the filter used by *Tian et al.* [2006], which is a combination of running means applied with different windows. They calculated an annual

cycle from only 7 years of data, in a region where the interannual variability is larger than the annual variability, and smoothed it with a 30-day running mean. They subtracted a 45-day running mean from a 15-day running mean, all applied to pentad data in an attempt to suppress high-frequency variability. Running means are an inapt way to filter time series owing to their poor spectral response [e.g., *von Storch and Zwiers*, 1999, p 386]. As a consequence, their multi-running-mean filter damps variance by about 15-30% even in the frequency range of interest, and has the undesirable feature, common to running means, of large variance at high frequency, especially at a period of 10 days where about 30% of variance is retained. By contrast, the bandpass filter used in our paper retains at full strength all variance at frequencies between 1/24 days and 1/51 days, and also strongly damps variance at all timescales shorter than about 20 days and longer than about 80 days, as desired. Their leading extended empirical orthogonal function (EEOF) had markedly lower variance explained - 6% for a single field - than ours at 39% for 6 fields or 34-48% for EEOFs of our individual fields, and this low variance is probably a consequence of this unsuitable filtering, which also renders the significance and robustness of their regression results rather questionable.

There are other measures of MJO variability besides filtered OLR; two examples are the indices based on empirical orthogonal functions (EOFs) of 200-hPa velocity potential calculated by the US Climate Prediction Center, and the Real-time Multivariate MJO indices of *Wheeler and Hendon* [2004]. These indices provide a somewhat different picture of the relative magnitude of the peak in MJO variability

during late 2002, but by any measure it is clearly one of the largest since the launch of the Terra satellite in late 1999. We present here a general view of variability over the period January 2001 – December 2004 and focus in detail on the time period 1 November 2002 through 28 February 2003, corresponding to the largest MJO activity of recent years (see shaded area in **Figure** 1).

Hovmöller plots of several relevant fields are shown in **Figure** 2. All fields are averaged over the latitude range 10˚S to 10˚N and are then bandpass filtered (20–70 days) to emphasize the intraseasonal timescales. Unfiltered OLR data (colors, panel a) are also shown for comparison. In the OLR field, several eastward-propagating features are evident in the eastern hemisphere but the western hemisphere -- especially the central and eastern Pacific ocean -- is characterized by high OLR with low variance, corresponding to persistently cloud-free conditions in this latitude band. Sea surface temperature, cloud fraction, cloud optical thickness, and cloud top temperature (not shown, but closely resembles cloud fraction and OLR) also have eastward-propagating features in the eastern hemisphere and only small anomalies in the western hemisphere, with high correlations among these fields (–0.60 between cloud top temperature and cloud optical thickness, 0.61 between cloud fraction and cloud optical thickness, and –0.90 between cloud top temperature and cloud fraction). Variability in SST associated with MJO has previously been noted [*Woolnough et al.,* 2000; *Hendon and Glick*, 1997]. AIRS low-level water vapor (averaged over levels 1-3, i.e., 1000, 925, and 850 hPa) similarly shows

evidence of eastward-propagating anomalies, but only in the eastern hemisphere. Previously we showed that near the tropical tropopause, water vapor anomalies extend into the western hemisphere [*Mote et al.* 2000].

The wind fields (e.g., at 850 hPa as shown in panel b) show strong anomalies well into the western hemisphere, which progress faster than those of the moist fields. Bandpass filtered zonal wind anomalies between the surface and about 500 hPa (not shown) are strongly correlated with those at 850 hPa; between 300 and 100 hPa, zonal wind anomalies are strongly anticorrelated with those at 850 hPa, reflecting the mid-tropospheric reversal in zonal winds associated with MJO [e.g., *Madden and Julian,* 1994].

3.1 Regressions of atmospheric state with OLR

In order to investigate the three-dimensional structure of these MJO variations, we regress temperature from AIRS and NCEP, and water vapor from AIRS, against the bandpass filtered OLR anomalies at 82.5°E, 0.0°N (**Figure** 1), the point with largest OLR amplitude. This regression analysis (**Figure** 3) shows that high correlations of temperature with MJO are found in much of the tropics and into the subtropics. Near the reference grid point (**Figure** 3b) the structure is complex, with convection (negative OLR) associated with warm anomalies in the middle troposphere (negative correlations

roughly 2–9 km) and cool anomalies at the surface and the upper troposphere. Ahead of the eastward-propagating MJO event, almost the entire tropical troposphere sees cool anomalies, while the surface sees warm anomalies which may be important in preconditioning the atmosphere for convection. The magnitude of anomalies near the reference point is slightly above 1°C per standard deviation in OLR, which is fairly large for the equatorial belt. These results may be compared with those of *Tian et al.* [2006], who showed longitude-height diagrams of temperature anomalies associated with different phases of the MJO computed by regressing AIRS temperature on the first EEOF of TRMM rainfall. Their lag-0 structure resembles our **Figure 3b**, with shallow warm anomalies around 150° E and a vertical dipole near the convective (rainfall) maximum. Whereas their figure emphasizes development of MJO anomalies in space-time, ours focuses on the structure of anomalies relative to the convective maximum. The mid-tropospheric warm anomalies near 80° E extend into the subtropics (**Figure 3d**).

Kiladis et al. [2001] performed lag regression of high-pass (<120 d) filtered tropopause temperatures at Koror (in the western Pacific) on radiosonde temperatures at Koror and found a large vertical variation near the tropopause. A –1 standard deviation (–2.2°C) anomaly at the tropopause was associated with a shallow cold anomaly extending only 1–2 km each side of the tropopause, and a small (~ 0.2°C) tropospheric warm anomaly extending the depth of the troposphere. In the stratosphere, the shallow cold anomaly lay below an even shallower warm anomaly above which, at pressures less than 50 hPa,

lay another cold anomaly. This structure, which changes with lag, could be a forced wave response to convection. In our analysis, the evolution of temperature anomalies with the passage of an MJO event would begin ~10 days ahead with warm anomalies in the boundary layer, followed by a reversal with strong cool anomalies in the boundary layer and warm anomalies in the mid-troposphere some days before the peak of the MJO event.

Examining panels d and e in **Figure 3**, or comparing panel a with panel c, to first order the MJO anomalies are symmetric about the equator. In the subtropics (panels a and c), there are strong anomalies across a range of longitudes, especially in the upper troposphere and lower stratosphere. During a mature positive MJO anomaly (negative OLR anomaly at the base point), cool anomalies in the subtropical upper troposphere and lower stratosphere (13–20 km) are found centered at about 60° and 240° longitude, above warm anomalies at 5–10 km. In between (roughly 100°–200° longitude), upper tropospheric warm anomalies overlie midtropospheric cool anomalies.

Atmospheric heating that is zonally symmetric about the equator would, in linear theory, produce eastward-propagating Kelvin wave responses most visible along the equator to the east of the heating and westward-propagating Rossby wave responses most visible off the equator to the northwest and southwest of the heating (e.g., *Gill,* 1980). By contrast, **Figure** 3 shows larger symmetric perturbations

to the *east* of the heating in the subtropics. More elaborate explanations of the MJO [e.g., *Lau and Peng,* 1987, or *Emanuel*, 1993] also do not predict such a strong response in the subtropics. The structure of anomalies between roughly 10˚S and 10˚N (**Figure** 3b) depends very little on latitude (not shown).

For NCEP (not shown, but see *Tian et al.* 2006), many of the features are similar, with the notable exception of the shallow warm anomaly ahead of the MJO event and the deep warm anomaly coincident with the reference point. Only at 10˚N does the shallow warm anomaly appear. Sparse observations in the tropics combined with the large Rossby radius of deformation conspire to deprive waves in the NCEP reanalysis of their full amplitude, particularly at small wavelengths (see, e.g., *Newman et al.* 2000).

In a mature phase of MJO at the 82˚E base point (**Figure** 3f), the entire tropical Indian Ocean region has warm anomalies in the midtroposphere while the central and eastern Pacific has cool anomalies. Surface anomalies (**Figure** 3g) are somewhat narrower in horizontal extent, and of opposite sign from the anomalies at 4.9km in the tropical Indian and western Pacific oceans.

Water vapor anomalies (**Figure** 4) have a different structure from the temperature anomalies, and not

solely because the mean vertical profile of water vapor drops by orders of magnitude. Even in the boundary layer there is little correspondence in the subtropics between moist/dry and warm/cool anomalies, and the water vapor anomalies are less symmetric with respect to the equator than the temperature anomalies. In the equatorial belt (**Figure** 4b), dry anomalies just west of the dateline are replaced by moist anomalies over a layer that grows deeper as the MJO convective maximum approaches. This tilted structure is quite different from the step change in temperature (**Figure 3b**). At the heart of the convective anomalies (**Figure** 4b, d) the middle troposphere is warm and moist. Just off the equator the surface dry anomalies deepen (**Figure** 4d). The moisture anomalies shown by *Tian et al.* [2006] are, likewise, rather different from their temperature anomalies.

For a thermodynamic perspective, we examine moist static energy anomalies, using

$$h' = c_p T + L_c q$$

where c_p is the specific heat of dry air and L_c is the latent heat of condensation, and T and q are the temperature and water vapor regression coefficients. The usual definition of moist static energy includes a term gz but since we are interested in tropical anomalies with respect to the mean state, we subtract the mean h which removes the gz term. **Figure** 5 shows the results; below about 5km the field is dominated by water vapor anomalies and above 5km by temperature anomalies. The tilted structure evident in **Figure** 4b is also quite striking here. Upper tropospheric anomalies are weaker than lower

tropospheric anomalies, especially near the equator, whereas for temperature they are of similar magnitude. But the key feature is the wedge of moist static energy that extends eastward from the convective maximum (**Figure** 5b). It appears that the buildup of moist static energy begins at low levels and gradually deepens until the whole lower troposphere up to 8km has large positive anomalies of moist static energy, at which point the convective anomalies grow. Ventilation by convection begins to deplete moist static energy at the surface (**Figure 5g**) so that by the time of maximum convection, a shallow layer (<2 km) of negative anomalies in moist static energy is in place and extends to ±20° latitude. The meridional structure has substantially more zonal asymmetry (compare panels a and c) than the structure of temperature anomalies (Figure 3).

3.2 Correlation of other fields with OLR

We have also performed correlation analysis on numerous fields from MODIS and other instruments over the 2001–2004 period of record. The fields from MODIS include cloud top temperature and pressure, cloud fraction retrieved two different ways, cloud optical thickness, cloud effective radius, liquid water path. We analyzed NCEP 700 hPa potential temperature, surface pressure, 600 and 700 hPa specific humidity (water vapor mixing ratio), and 700 hPa vector wind; AMSR water vapor path, liquid water path, rain, SST, and windspeed; Quikscat-NCEP blended surface wind; TMI water vapor path, cloud liquid water path, and blended TMI-Reynolds SST.

For many of these fields, the correlation map resembles random noise or has very weak (0.2) correlations even near the OLR reference point: cloud optical thickness, cloud effective radius, liquid water path from MODIS, AMSR, and TMI; NCEP 700 hPa potential temperature; MODIS cloud fraction of water clouds; and SST, owing partly to the SST anomalies being roughly in quadrature with OLR (Figure 2).

Some fields, however, are more clearly involved in the MJO (**Figure** 6). Cloud top temperature, of course, is very strongly related to OLR so the variability of cloud top temperature is strongly related to the variability of OLR. Peak correlation is 0.45. Unfiltered OLR anomalies are roughly ± 100 W/m^2; bandpass filtered anomalies are ± 50 W/m^2, and OLR anomalies are roughly linearly related to anomalies of cloud top temperature with a slope of 1.4 Wm^{-2}/K. Cloud fraction, whose distribution is very similar to that of cloud top temperature in both the time mean [*Mote and Frey,* 2006] and also in the period of high MJO activity (**Figure** 2), also varies strongly with MJO, and its correlation with the OLR reference time series is –0.49. Clouds are more abundant and their tops are colder when the MJO is at its convective maximum, and the peak values are both located at the location of the OLR reference time series, for obvious reasons. During a peak in MJO convective activity, cloud top temperature throughout the Indian Ocean experiences negative anomalies, and cloud fraction positive anomalies,

with the area of statistically significant correlations being roughly two-thirds the size of Australia.

For NCEP surface pressure, which over land varies mostly with elevation, MJO is associated with an elongated tropical low pressure anomaly that is shifted somewhat to the east of the OLR reference point. It is also associated with weak positive (high pressure) anomalies in the subtropical western Pacific of both northern and southern hemispheres.

Patterns of the moisture fields (Figure 6, bottom two rows) have some interesting properties. Mid-tropospheric moisture (NCEP 700 hPa specific humidity q) and AMSR water vapor path (WVP) have different mean distributions: q has local maxima in the convective regions of the western Pacific, South America, and Africa whereas AMSR WVP is more zonally elongated along the ITCZ with less distinction between adjacent convective areas. Midtropospheric moisture is elevated by convection, so moist features at 700 hPa are more closely linked to convection. On the other hand, WVP represents column water vapor which is dominated by lowest levels and corresponds closely with SST; *Mote and Frey* [2006] noted that the spatial correlation between clear-sky WVP and SST exceeds 0.8 in the subtropics and is about 0.66 in the tropics. The correlations of AMSR WVP and NCEP q with the OLR reference time series also have different patterns. With minimum OLR at the reference point, the q field has positive anomalies over most of the Indian ocean (with maximum correlation well to the east of the reference point) and negative anomalies over much of the Pacific, whereas AMSR WVP has

a narrower maximum located not quite so far east. The maximum correlation for each is about 0.3.

Additional insight comes from the Quikscat-NCEP wind field (**Figure** 7). The disturbances associated with the MJO produce strong westerly anomalies in the equatorial Indian Ocean, including well east of the OLR reference point. That is, the surface wind field has a maximum convergence about 2000km east of the maximum OLR anomaly. The divergence field anomalies associated with MJO are dominated by $\partial u/\partial x$, convergence of the zonal component of the wind. Fairly strong circulation anomalies in the subtropical western Pacific are associated with the high pressure anomalies shown in the previous figure. There also appears to be a response in higher latitudes of both the eastern Pacific and Atlantic basins in both hemispheres.

4. Multivariate extended empirical orthogonal functions

Empirical orthogonal function (EOF) analysis is often used in the atmospheric sciences for finding coherent spatial patterns in noisy data. Extended EOFs (EEOFs) [*Weare and Nasstrom,* 1982] are useful for identifying coherent patterns of spatiotemporal variations, and we developed MEEOFs (multivariate EEOFs) [*Mote et al.,* 2000] for identifying coherent spatiotemporal variations among several fields. The MEEOF calculation is performed by concatenating longitude-lag vectors for each of the *F* variables shown in **Figure** 2. The order of the variables is immaterial, but they must be

normalized so that the MEEOFs reflect physical variations and not the unit used to measure the variables. Once the MEEOFs are calculated, they can be separated into the corresponding component for each variable, here called $EEOF_m$; the $EEOF_m$ then illustrate each field's response to coherent variations across all the fields.

The first two MEEOFs (consisting of the five constituent $EEOF_m$) are shown in **Figure** 9. These two MEEOFs are a conjugate pair, as are the next two (not shown); all four are dominated by eastward moving features, with maximum variance between 60° and 180° east longitude. Conjugate pairs of EOFs are typical for propagating features; their spatial structures are similar but one quarter cycle out of phase, and their principal component time series are also typically a quarter cycle out of phase. The characteristic timescale is approximately 45 days, and the first pair of MEEOFs explains 73.8% of the variance.

In the eastern hemisphere, coherent anomalies of OLR (top row) are coincident with cloud top temperature and oppositely signed anomalies in cloud fraction (third and fourth rows). The 850-hPa wind anomalies (second row) lead the cloud anomalies by approximately 50° longitude or 12–15 days. Large-scale convergence (not shown), approximated by $\partial u/\partial x$, reaches a maximum value approximately where u=0 and OLR is a minimum, reflecting the large-scale relationship between convection and convergence (see also *Madden and Julian* 1994).

Intraseasonal anomalies in the wind field continue into the eastern Pacific at higher phase speed, a fast dry Kelvin wave disconnected from convection. That the relationship is somewhat stronger for negative lag (leading the variations that dominate the $EEOF_m$) than for positive lag may be an artifact of the strong MJO anomaly at the beginning of the analysis period (see top of **Figure** 2) rather than a physical relationship.

AIRS low-level water vapor (**Figure** 9, third row, defined as in Fig 2) is roughly in quadrature with OLR, as expected from the phase relationships in Figure 4. The build-up of low-level water vapor precedes, and is required for, the MJO convective maximum. Large stationary variations in low-level water vapor appear in the eastern Pacific in phase with those in the Indian ocean (see also Figure 4g); this extension beyond the dateline is somewhat surprising, given the lack of MJO variability in clouds and midtropospheric moisture (not shown) in the western hemisphere. Evidently the low-level wind anomalies (Figure 7) contribute to moisture anomalies even if no clouds result yet. But those eastern Pacific moisture anomalies do not appear to propagate.

Cloud fraction anomalies (Figure 9, fifth row) also vary quite similarly to those of OLR and cloud top temperature. Cloud optical thickness, however, shows quite different intraseasonal variability from the other fields. In the Indian Ocean, anomalies propagate eastward but at half the speed. In the western

Pacific the anomalies have an intraseasonal component but do not appear to be linked to propagating anomalies. A closer examination of the relationship between cloud optical thickness, cloud top temperature, and cloud fraction in the MODIS L2 data suggests that cloud optical thickness is seldom retrieved for cloud fraction less than 1 at the pixel scale (5km×5km) especially for low clouds (M. Zelinka, personal communication, 2008). Whether this retrieval failure is related to the unusual behavior of the intraseasonal cloud optical thickness anomalies is unclear. Incidentally, separate EEOF analysis of each field reveals that the leading modes are quite similar to those shown here, so it is not simply a matter of the projection of the MJO anomalies in other fields onto the cloud optical thickness anomalies.

5. Discussion and Conclusions

The analysis presented here links dynamical fields such as temperature and winds with clouds and water vapor. Coherent three-dimensional evolution of convective events in the Indian and Western Pacific proceeds as follows. Ahead of the event, low-level convergence anomalies produce a shallow warm layer that builds up moist enthalpy. These features are seen in **Figures** 5e, 7, and 9. As deep convection develops, strong heating of the middle troposphere (2–10 km) and cooling of the upper troposphere occurs, and column water vapor increases owing mainly to the buildup of water vapor in the lowest few km of the atmosphere. Finally, cloud fraction and cloud top temperature anomalies

440 develop. This sequence is roughly as described in the MJO model of *Raymond* [2001], with specified SST. Note that in his model the fluctuations in surface fluxes, which precede the change in atmospheric structure, are driven not by SST variations but by changes in winds. In our analysis there is virtually no correlation between daily SST (from either TMI or AMSR) and MJO OLR anomalies, bolstering a dynamically induced mechanism like that of *Raymond* [2001] rather than an SST feedback 445 onto the eastward-propagating atmospheric anomalies.

The pattern of observed surface wind anomalies (**Figure 7**) departs, especially in the Indian Ocean, from the schematic diagram of MJO-related surface wind presented by *Rui and Wang* [1990]. Their diagram showed two lower level cyclonic circulation features west and poleward of the convective 450 maximum in the Indian Ocean. In the Quikscat data the circulation pattern in the Indian Ocean shows little evidence either of symmetry across the equator or of cyclonic flow. The anomalous inflow from the south is in the same direction - northwestward - as the mean flow, with a sharp eastward turn near the equator. In fact the MJO-related flow near the equator is quite narrowly confined to a sharp westerly jet, as is the easterly flow in the western Pacific. Both the radius of curvature of the flow and 455 the narrowness of the jet are surprisingly sharp features for tropical wind anomalies, and are not found in the NCEP/NCAR reanalysis surface winds (not shown). Regression of OLR on surface winds give anomalies of 2-3 m/s per standard deviation in OLR for Quikscat but only 0.5-1 m/s for NCEP.

The phase relationship between OLR and low-level wind reveals a great deal about the dynamical mechanism of the MJO. *Zhang* [2005] summarizes the relationship between low-level wind convergence and MJO convection predicted by various theories of the MJO with four possible models (his Figure 6). Our Quikscat results most closely resemble his model II, with strong westerly winds coinciding with the convective maximum and the maximum in convergence occurring well to the east of the convection; although Zhang states that model II is more common in the Pacific, we observe that structure in both the Indian and Pacific Oceans. By contrast, the NCEP/NCAR surface and lower tropospheric winds (**Figure** 8) show convergence at the OLR minimum both for the Indian and the Pacific oceans, with largest wind anomalies found east of the Indian Ocean base point (Model III) and west of the West Pacific base point (Model I). Evidently the dynamics and convective parameterizations of the NCEP/NCAR reanalysis model are inadequate to produce the vigorous fine-scale features observed by Quikscat.

Not all moist fields respond in concert to the MJO variations. For example, liquid water path, fractional area covered by water clouds, and AMSR rain are uncorrelated with the OLR base point. Cloud optical thickness anomalies exhibit intraseasonal properties but propagate more slowly than the MJO features (Figures 2 and 9). Even without a clear signal in these fields, this paper shows a more complete view of MJO events using a wide range of datasets.

Acknowledgments

This research was supported by NASA Contracts NNH04CC63C and NNH08CC72C, and by NorthWest Research Associates Inc.

References

Barnes, W.L., T.S. Pagano, and V.V. Salomonson (1998), Prelaunch characteristics of the Moderate Resolution Imaging Spectroradiometer (MODIS) on EOS-AM1, *Transactions on Geoscience and Remote Sensing, 36,* 1088–1100.

Bond, N.A., and G.A. Vecchi (2003), On the Madden Julian Oscillation and precipitation in Oregon and Washington, *Weather and Forecasting, 18,* 600–613, doi: 10.1175/1520–0434.

Cho, H.-R., K. Fraedrich, and J.T. Wang (1994), Cloud clusters, Kelvin wave-CISK, and the Madden-Julian Oscillation in the equatorial troposphere, *J. Atmos. Sci., 51,* 68–76.

Eguchi, N., and M. Shiotani (2004), Intraseasonal variations of water vapor and cirrus clouds in the tropical upper troposphere, *J. Geophys. Res., 109,* doi:10.1029/2003JD004314.

Emanuel, K.E. (1993),T he effect of convective response time on WISHE modes, *J. Atmos. Sci., 50,*

1763–1775.

EOS (2000), EOS Data Products Handbook, vol. 2, pp 21–22, quoted on the AIRS web site www.aqua.nasa.gov/AIRS3.html

Field, P. R. and R. Wood (2007), Precipitation and cloud structure in midlatitude cyclones, *J. Clim., 20,* 233–254, doi 10.1175/JCLI3998.1

Gill, A.E. (1980), Some simple solutions for the heat-induced tropical circulation, *Q.J. Roy. Meteorol. Soc., 106,* 447–462.

Hendon, H.H., and J. Glick (1997), Intraseasonal Air–Sea Interaction in the Tropical Indian and Pacific Oceans, *J. Clim., 10,* 647-661.

Kalnay, E., et al. (1996), The NCEP/NCAR 40–Year Reanalysis Project, *Bull. Amer. Meteor. Soc., 77,* 437–471.

Kiladis, G.N., K.H. Straub, G.C. Reid, and K.S. Gage (2001), Aspects of interannual and intraseasonal variability of the tropopause and lower stratosphere, *Q. J. R. Meteorol. Soc., **127,*** 1961–1983.

King, M.D., W.P. Menzel, Y.J. Kaufman, D. Tanré, B.-C. Gao, S. Platnick, S.A. Ackerman, L.A. Remer, R. Pincus, and P.A. Hubanks (2003), Cloud and aerosol properties, precipitable water, and profiles of temperature and water vapor from MODIS, *IEEE Transactions on Geoscience and Remote Sensing, 41,* 442–458, doi: 10.1109/TGRS.2002.808226.

Kistler, R., et al. (2001), The NCEP-NCAR 50-Year Reanalysis: Monthly means CD-ROM and documentation, *Bull. Amer. Meteor. Soc., 82,* 247–267.

Lau, K.-M., and L. Peng (1987), Origin of low-frequency (intraseasonal) oscillations in the tropical atmosphere. Part I: basic theory, *J. Atmos. Sci., 44,* 950–972.

Lau, K.-M., and P.H. Chan (1983), Short-term climate variability and atmospheric teleconnections from satellite-observed outgoing longwave radiation simultaneous relationships, *J. Atmos. Sci., 40,* 2735–2750.

Liebmann, B., and C.A. Smith (1996), Description of a complete (interpolated) outgoing longwave radiation dataset, *Bull. Amer. Meteor. Soc., 77,* 1275–1277.

Lin, J-L., and B.E. Mapes (2004), Radiation budget of the tropical intraseasonal oscillation, *J. Atmos. Sci., 61,* 2050-2062.

Lo, F., and H.H. Hendon (2000), Empirical Prediction of the Madden-Julian Oscillation, *Mon. Wea. Rev.* **128,** 2528–2543.

Madden, R.A., and P.R. Julian (1971), Description of a 40–50 day oscillation in the zonal wind in the tropical Pacific, *J. Atmos. Sci., 28,* 702–708.

Madden, R.A., and P.R. Julian (1994), Observations of the 40–50 day tropical oscillation – a review, *Mon. Wea. Rev., 122,* 814–837.

Maloney, E.D., and D.L. Hartmann (2000), Modulation of hurricane activity in the Gulf of Mexico by the Madden-Julian oscillation, *Science, 287,* 2002–2004.

McPhaden, M.J. (1999), Genesis and evolution of the 1997–98 El Niño, *Science, 283,* 950–954.

Mote, P.W., and R. Frey (2006), Variability of clouds and water vapor in low latitudes: view from Moderate Resolution Imaging Spectroradiometer (MODIS), *J. Geophys. Res., 111,* D16101, doi

555 10.1029/2005JD006791.

Mote, P.W., H.L. Clark, T.J. Dunkerton, R.S. Harwood, and H.C. Pumphrey (2000), Intraseasonal variations of water vapor in the tropical upper troposphere and tropopause region, *J. Geophys. Res., 105,* 17,457–17,470.

560

Newman, M., P.D. Sardeshmukh, and J.W. Bergman (2000), An Assessment of the NCEP, NASA, and ECMWF Reanalyses over the Tropical West Pacific Warm Pool, *Bull. Amer. Meteor. Soc., 81,* 41–48.

Platnick, S., M.D. King, S.A. Ackerman, W.P. Menzel, B.A. Baum, J.C. Riédi, and R.A. Frey (2003),
565 The MODIS cloud products: Algorithms and examples from Terra, *IEEE Transactions on Geoscience and Remote Sensing, 41,* 459–473, doi: 10.1109/TGRS.2002.808301.

Raymond, D.J. (2001), A new model of the Madden-Julian Oscillation, *J. Atmos. Sci., 58,* 2808–2819.

570 Rui, H., and B. Wang (1990), Development characteristics and dynamic structure of tropical intraseasonal convection anomalies, *J. Atmos. Sci., 47,* 357–379.

Sassi, F., M. Salby, H.C. Pumphrey, and W.G. Read (2002), Influence of the Madden-Julian

Oscillation on upper tropospheric humidity, *J. Geophys. Res., 107,* doi:10.1029/2001JD001331.

Stephens, G.L., et al. (2002), THE CLOUDSAT MISSION AND THE A-TRAIN: A New Dimension of Space-Based Observations of Clouds and Precipitation, *Bull. Amer. Meteorol. Soc., **83,*** doi: 10.1175/BAMS-83-12-1771.

Tian, B., D.E. Waliser, E.J. Fetzer, B.H. Lambrigtsen, Y.L. Yung, and B. Wang (2006), Vertical Moist Thermodynamic Structure and Spatial-Temporal Evolution of the MJO in AIRS Observations, *J. Atmos. Sci., 63,* 2462–2485.

von Storch, H.V., and F.W. Zwiers (1999), *Statistical analysis in climate research,* 484 pp, Cambridge University Press, Cambridge, UK.

Wang, B., and H. Rui (1990), Synoptic climatology of transient tropical intraseasonal convective anomalies: 1975–1985, *Meteorol. Atmos. Phys.,* 44, 43-61.

Weare, B.C., and J.S. Nasstrom (1982), Examples of extended empirical orthogonal function analysis, *Mon. Wea. Rev., 110,* 481–485.

Wentz, F. J. (1997), A well calibrated ocean algorithm for special sensor microwave/imager, *J. Geophys. Res., 104,* 8703–8717.

Wentz, F.J., and T. Meissner (2000), *AMSR Ocean Algorithm. Algorithm Theoretical Basis Document Tech. Rep. version 2,* Remote Sensing Systems, Santa Rosa, CA, 59 pp.

Wentz, F. J., and D. K. Smith (1999), A model function for the ocean normalized radar cross section at 14 GHz derived from NSCAT observations, *J. Geophys. Res., 104,* 11,499–11,514.

Wentz, F.J., and R. W. Spencer (1998), SSM/I rain retrievals within a unified all-weather ocean algorithm, *J. Atmos. Sci., 55,* 1613–1627.

Wheeler, M.C., and H.H. Hendon (2004), An all-season real-time multivariate MJO index: Development of an index for monitoring and prediction, *Mon. Wea. Rev.,* 132, 1917-1932.

Woolnough, S.J., J.M. Slingo, and B.J. Hoskins (2000), The relationship between convection and sea surface temperature on intraseasonal timescales, *J. Clim., 13,* 2086-2104.

Yang, P., L. Zhang, G. Hong, S.L. Nasiri, B.A. Baum, H.L. Huang, M.D. King, and S. Platnick (2007),

Differences between collection 4 and 5 MODIS ice cloud optical/microphysical products and their impact on radiative forcing simulations, *IEEE Transactions on Geoscience and Remote Sensing*, 45(9), 2886-2899.

615

Zhang, C. (2005), Madden-Julian Oscillation, *Rev. Geophys., 43,* doi: 10.1029/2004RG000158.

Figure 1

Bandpass filtered (20–70 day) outgoing longwave radiation at the location of greatest OLR variance, 82.5˚E, 0˚N. The shaded box indicates the large-MJO period that is a special focus of this paper, and the dotted line indicates the maximum value of filtered OLR in November 2002.

Figure 2

Hovmöller (longitude-time) contour plots of the fields indicated. The solid contours overlaid on each panel are the bandpass (20–70 d) filtered OLR, with contour interval 10 Wm^{-2}. The low-level water vapor is an average of AIRS water vapor on levels 1-3 (1000, 925, 850 hPa). Continents are shaded gray in the SST panel.

Figure 3

Regression of AIRS temperature with OLR over the 10/01/02 – 03/30/06 period of record. The reference time series of OLR was bandpass filtered, and the the location is indicated by vertical lines in the top six panels and by a star in the bottom two. Contour interval 0.03 $K(Wm^{-2})^{-1}$.

Figure 4

As in Figure 3 but for water vapor, contour interval 25 $ppmv(Wm^{-2})^{-1}$.

Figure 5

As in Figure 3 but for moist static energy, contour interval 35 J $kg^{-1}(Wm^{-2})^{-1}$. Blue (red) colors are positive (negative) MSE anomalies for a minimum in OLR.

Figure 6

Mean fields (left) and correlations (right) with lowpass filtered OLR at the Indian Ocean base point. The sign of the correlations have been reversed to show the fields at the peak of a convective event (low OLR).

Figure 7

Quikscat surface winds: mean (top) and regression with lowpass filtered OLR at the Indian Ocean base point (bottom).

Figure 8. Regression of NCEP equatorial wind (longitude-altitude projection) on OLR for base points, indicated by vertical lines, in the Indian Ocean (top) and Western Pacific Ocean.

Figure 9

First two mEEOFs of the six fields shown in Figure 2 (see text for explanation). Black curves overlaid on each panel trace features in the top left panel. Contour intervals are in dimensionless units.

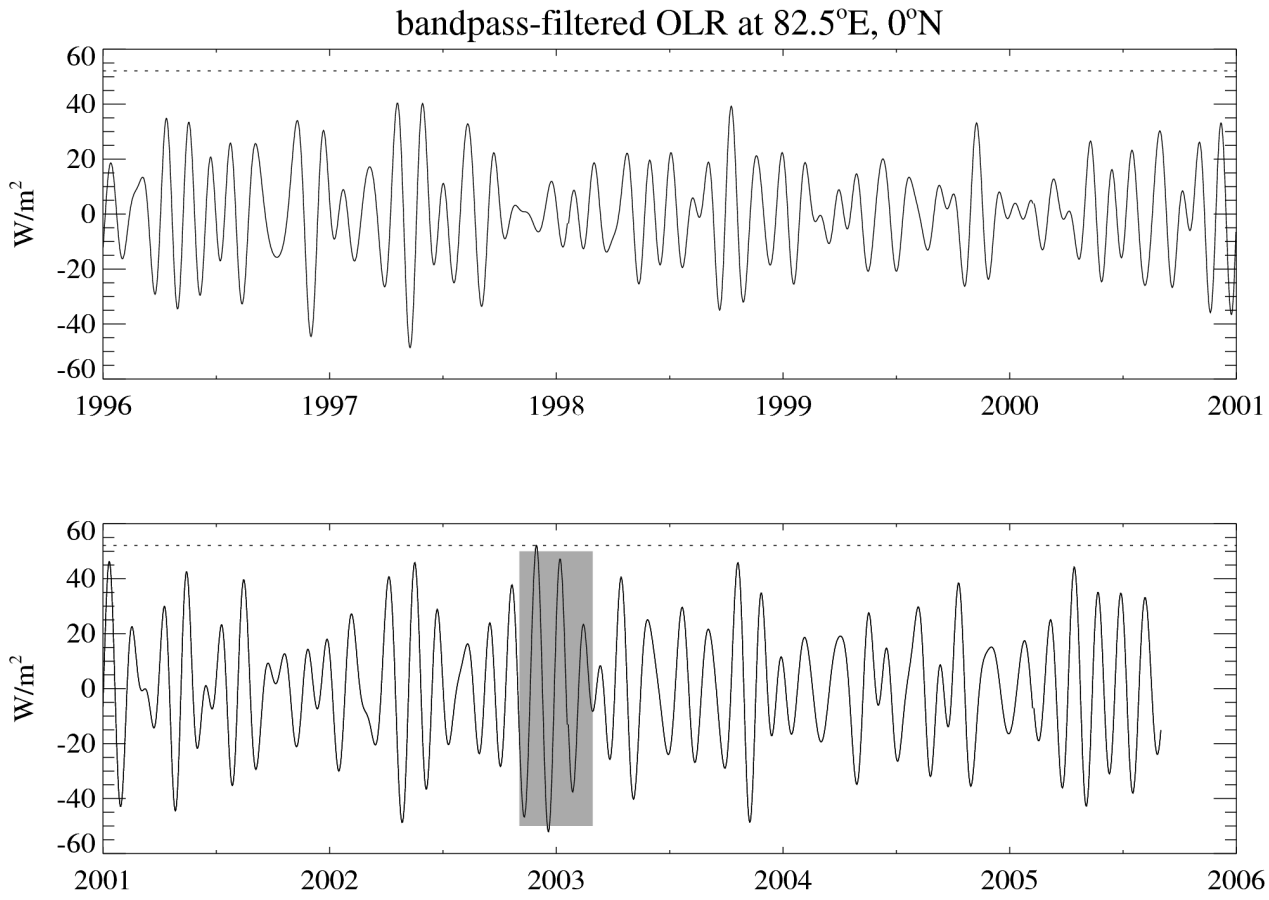

Figure 1

Bandpass filtered (20–70 day) outgoing longwave radiation at the location of greatest OLR variance, 82.5°E, 0°N. The shaded box indicates the large-MJO period that is a special focus of this paper, and the dotted line indicates the maximum value of filtered OLR in November 2002.

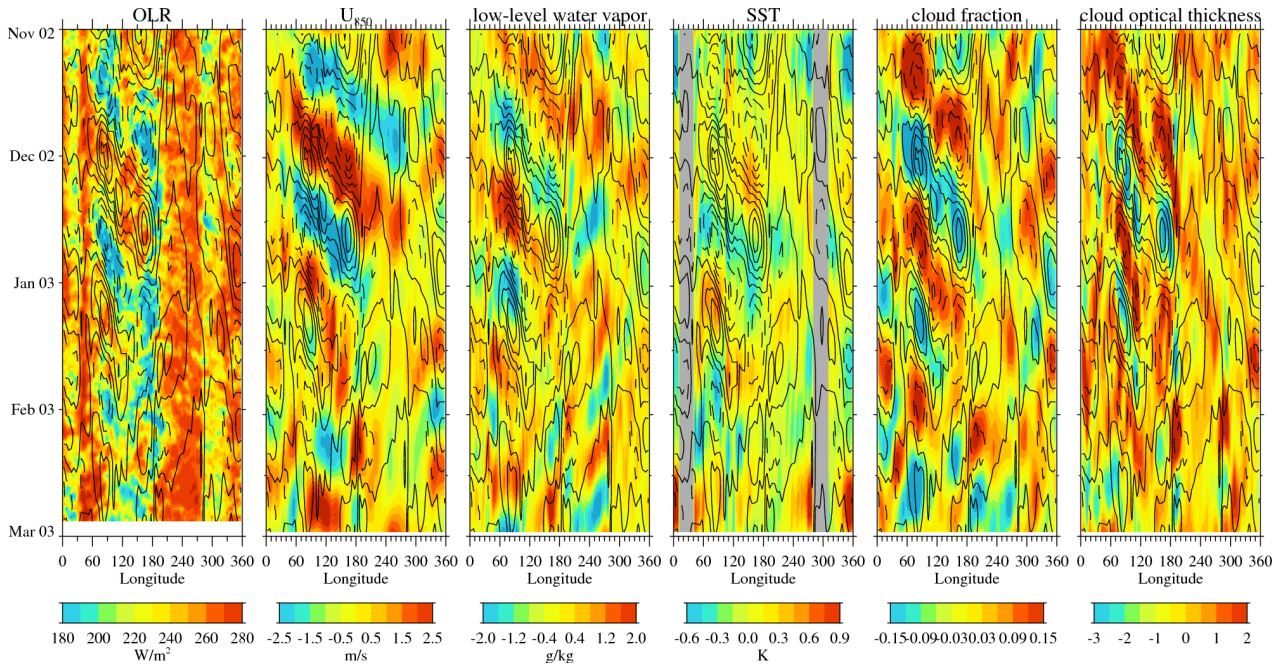

Figure 2

Hovmöller (longitude-time) contour plots of the fields indicated. The solid contours overlaid on each panel are the bandpass (20–70 d) filtered OLR, with contour interval 10 Wm^{-2}. The low-level water vapor is an average of AIRS water vapor on levels 1-3 (1000, 925, 850 hPa). Continents are shaded gray in the SST panel.

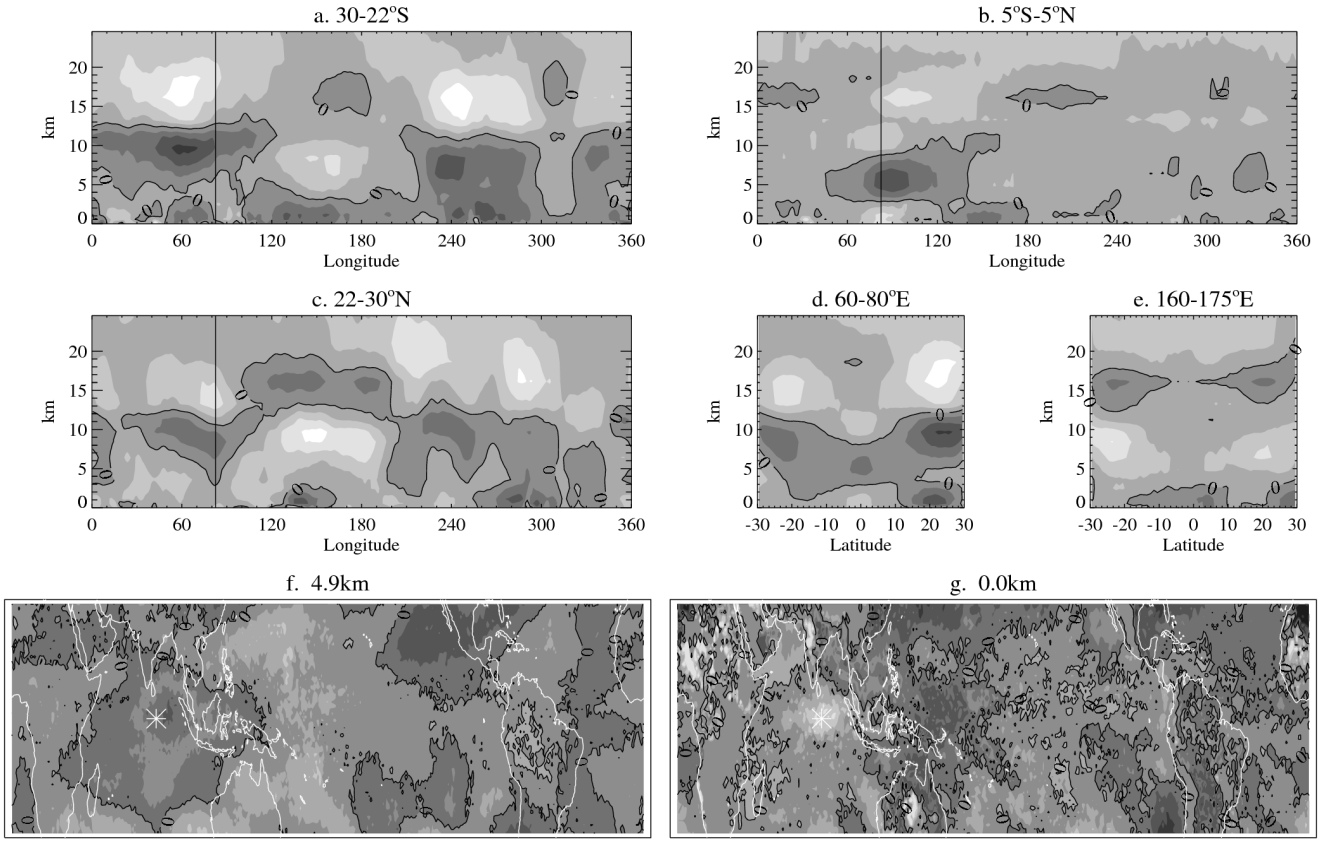

Figure 3

Regression of AIRS temperature with OLR over the 10/01/02 – 03/30/06 period of record. The reference time series of OLR was bandpass filtered, and the the location is indicated by vertical lines in the top six panels and by a star in the bottom two. Contour interval 0.03 $K(Wm^{-2})^{-1}$.

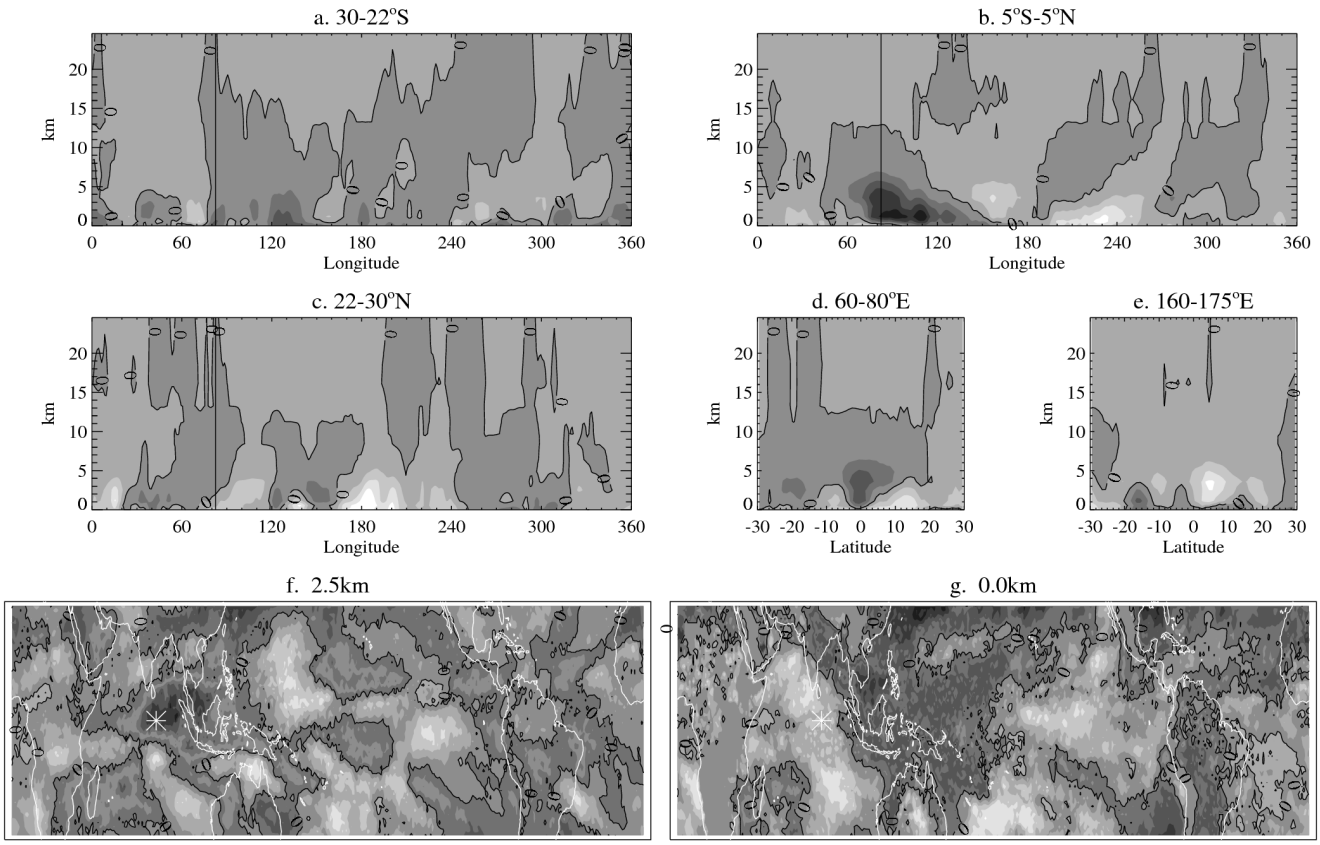

Figure 4

As in Figure 3 but for water vapor, contour interval 25 ppmv$(Wm^{-2})^{-1}$.

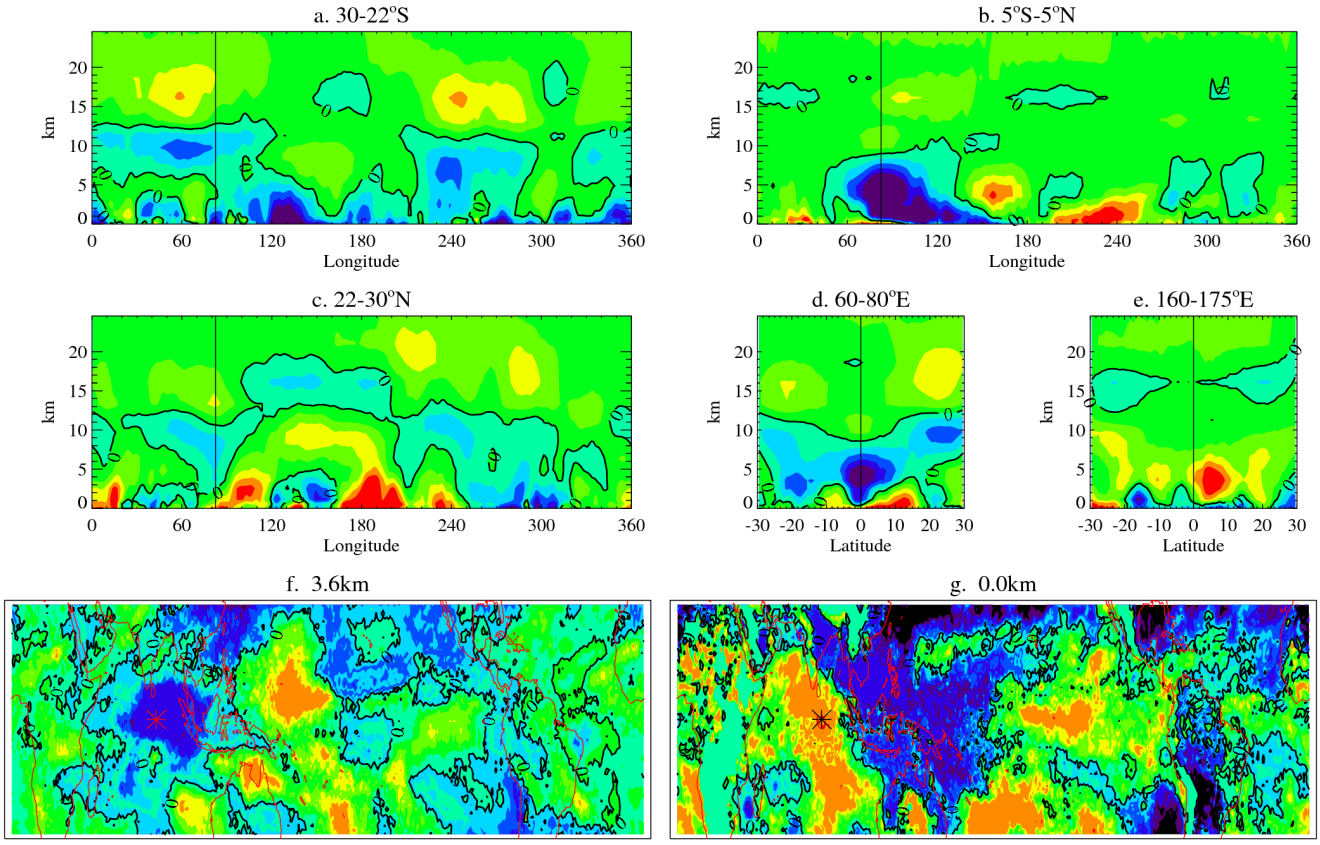

Figure 5

As in Figure 3 but for moist static energy, contour interval 35 J $kg^{-1}(Wm^{-2})^{-1}$. Blue (red) colors are positive (negative) MSE anomalies for a minimum in OLR.

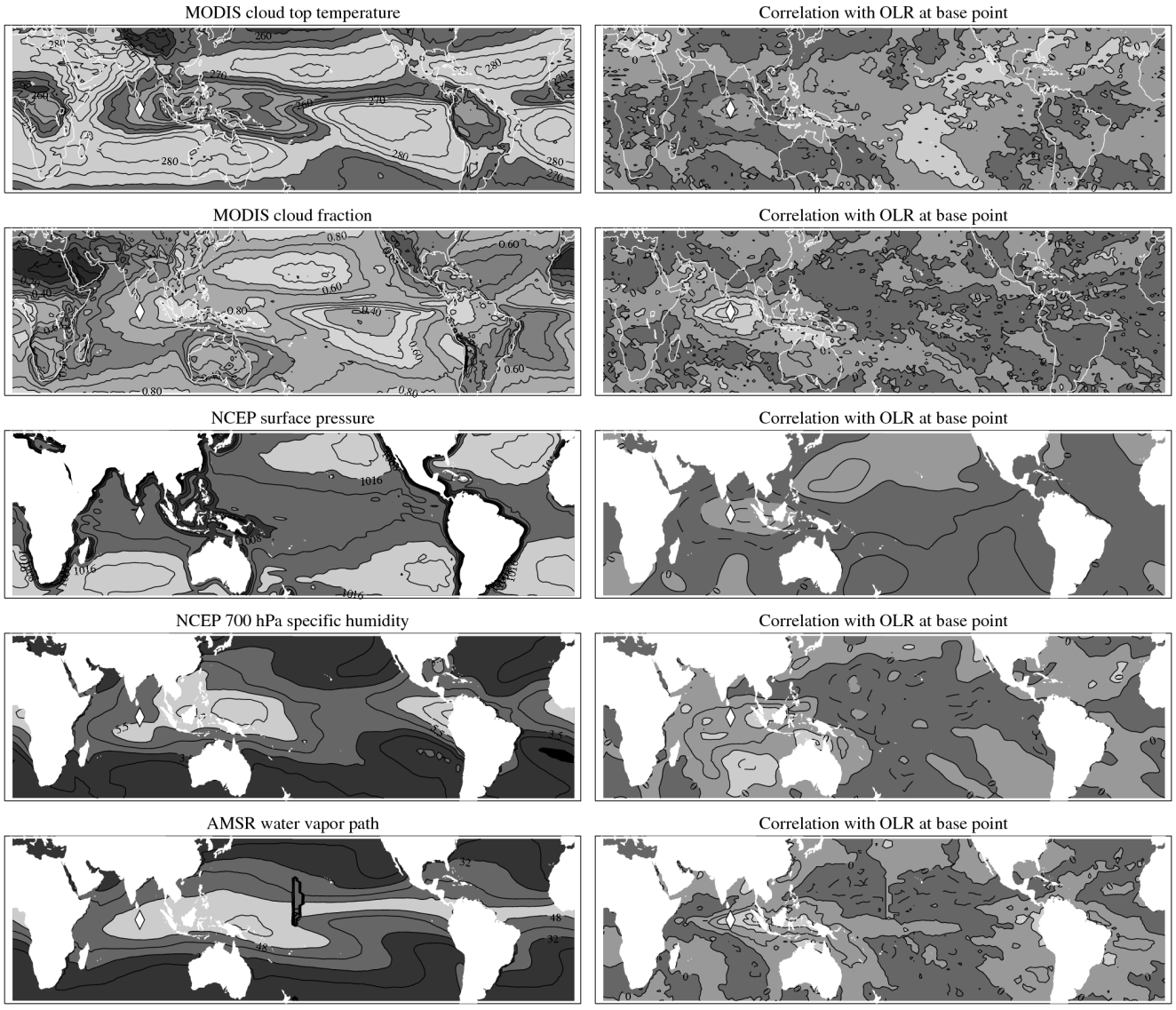

Figure 6

Mean fields (left) and correlations (right) with lowpass filtered OLR at the Indian Ocean base point.

The sign of the correlations have been reversed to show the fields at the peak of a convective event

(low OLR).

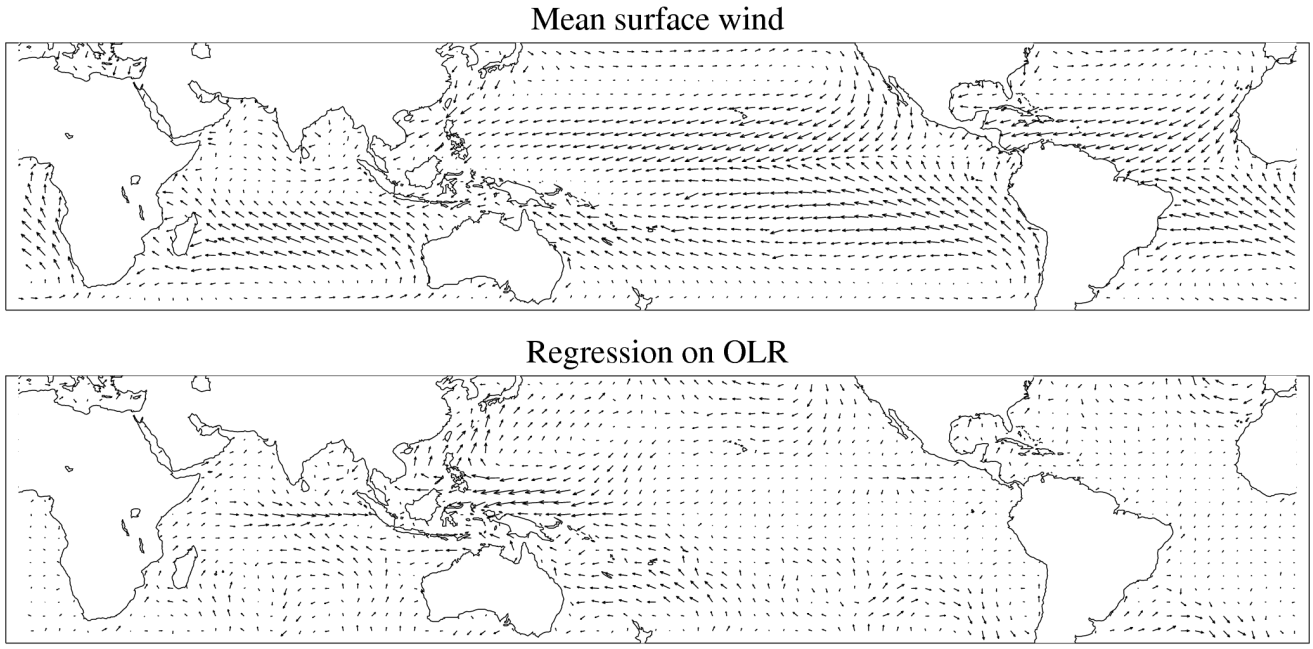

Figure 7

Quikscat surface winds: mean (top) and regression with lowpass filtered OLR at the Indian Ocean base point (bottom).

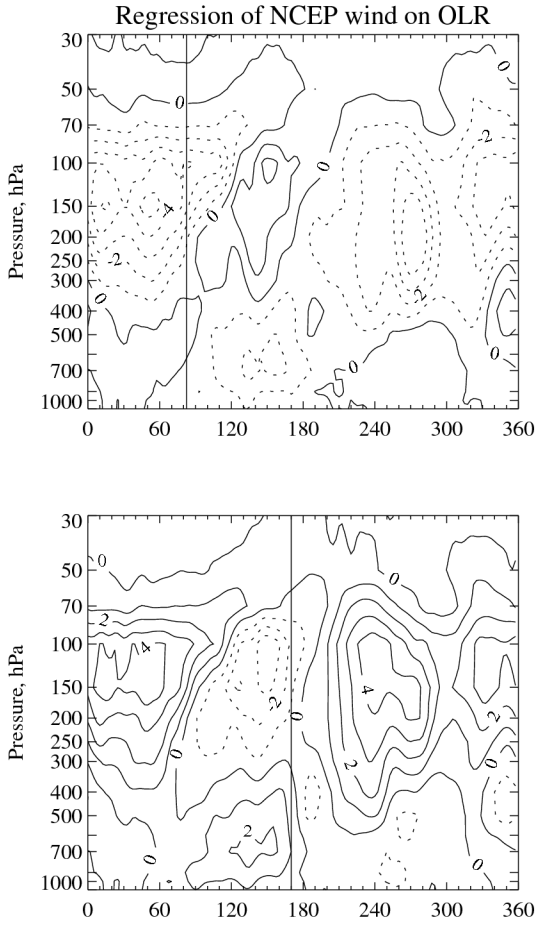

Figure 8. Regression of NCEP equatorial wind (longitude-altitude projection) on OLR for base points, indicated by vertical lines, in the Indian Ocean (top) and Western Pacific Ocean.

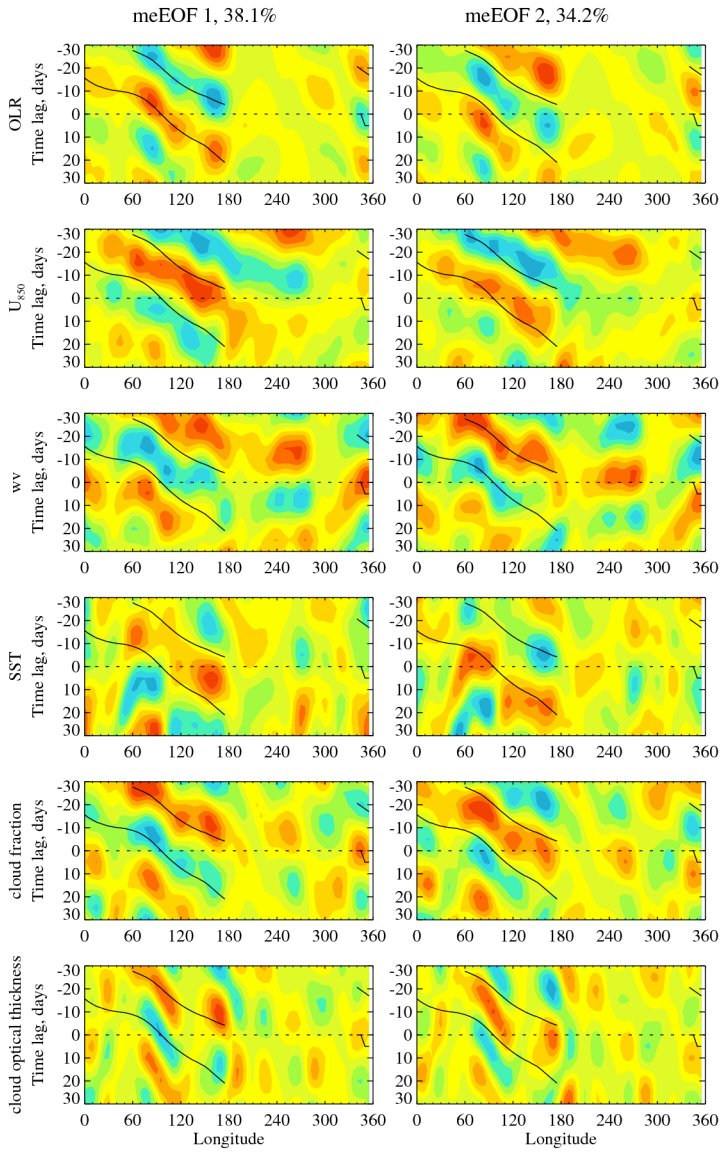

Figure 9

First two mEEOFs of the six fields shown in Figure 2 (see text for explanation). Black curves overlaid on each panel trace features in the top left panel.